Stray-light analyses of the multielement telescope for imaging and spectroscopy coronagraph on Solar Orbiter

Optical Engineering

OpticalEngineering.SPIEDigitalLibrary.org

Stray-light analyses of the multielement telescope for imaging and spectroscopy coronagraph on Solar Orbiter

Paolo Sandri
Silvano Fineschi
Marco Romoli
Matteo Taccola
Federico Landini
Vania Da Deppo
Giampiero Naletto
Danilo Morea
Denis Naughton
Ester Antonucci

SPIE.

Paolo Sandri, Silvano Fineschi, Marco Romoli, Matteo Taccola, Federico Landini, Vania Da Deppo, Giampiero Naletto, Danilo Morea, Denis Naughton, Ester Antonucci, "Stray-light analyses of the multielement telescope for imaging and spectroscopy coronagraph on Solar Orbiter," *Opt. Eng.* **57**(1), 015108 (2018), doi: 10.1117/1.OE.57.1.015108.

Stray-light analyses of the multielement telescope for imaging and spectroscopy coronagraph on Solar Orbiter

Paolo Sandri,[a] Silvano Fineschi,[b,*] Marco Romoli,[c] Matteo Taccola,[d] Federico Landini,[e] Vania Da Deppo,[f] Giampiero Naletto,[g,f] Danilo Morea,[h] Denis Naughton,[†] and Ester Antonucci[b]
[a]OHB Italia, Osmannoro, Florence, Italy
[b]Istituto Nazionale di Astrofisica–Astrophysical Observatory of Torino, Turin, Italy
[c]University of Florence, Department of Physics and Astronomy, Firenze, Italy
[d]European Space Agency–European Space Research and Technology Center, Noordwijk, The Netherlands
[e]Istituto Nazionale di Astrofisica–Astrophysical Observatory of Arcetri, Firenze, Italy
[f]Consiglio Nazionale delle Ricerche–Istituto Di Fotonica E Nanotecnologie Sede Di Padova, Laboratorio LUXOR, Padova, Italy
[g]University of Padova, Department of Physics and Astronomy, Padova, Italy
[h]OHB Italia, Milano, Italy

Abstract. The modeling of the scattering phenomena for the multielement telescope for imaging and spectroscopy (METIS) coronagraph on board the European Space Agency Solar Orbiter is reported. METIS is an inverted occultation coronagraph including two optical paths: the broadband imaging of the full corona in linearly polarized visible-light (580 to 640 nm) and the narrow-band imaging of the full corona in the ultraviolet Lyman-α (121.6 nm). METIS will have the unique opportunity of observing the solar outer atmosphere as close to the Sun as 0.28 AU and from up to 35 deg out-of-ecliptic. The stray-light simulations performed on the UV and VL channels of the METIS analyzing the contributors of surface microroughness, particulate contamination, cosmetic defects, and diffraction are reported. The results obtained with the nonsequential modality of Zemax OpticStudio are compared with two different approaches: the Monte Carlo ray trace with Advanced Systems Analysis Program (ASAP®) and a semianalytical model. The results obtained with the three independently developed approaches are in considerable agreement and show compliance to the requirement of stray-light level for both the UV and VL channels. [DOI: 10.1117/1.OE.57.1.015108]

Keywords: modeling scattering; multielement telescope for imaging and spectroscopy coronagraph; stray light; surface microroughness; diffraction; particulate contamination; cosmetics.

Paper 161176P received Jul. 26, 2016; accepted for publication Oct. 10, 2017; published online Jan. 25, 2018.

1 Introduction

The modeling of scattering phenomena represents an important topic in diverse areas of science and engineering. In some fields, such as space applications, the total amount of scattered radiation is of primary concern for stray-light assessment and minimization.

This paper reports the results of the stray-light analyses performed for the multielement telescope for imaging and spectroscopy (METIS) coronagraph aboard the Solar Orbiter mission of European Space Agency for the study and characterization of the solar corona[1] and presented at an SPIE conference.[2] The observation of the solar corona requires a coronagraph that is a telescope equipped with a system to occult the light from the sun disk. METIS is designed to perform simultaneous imaging in the visible light (VL) spectrum from 580 to 640 nm and a narrow-band (FWHM = 10 nm) imaging at the ultraviolet (UV) wavelength of 121.6 nm. To meet the harsh thermal requirements of the mission, the design of METIS is based on an innovative occulting concept with the entrance aperture acting as an inverted external occulter (IEO).[3–5]

Every coronagraph METIS requires highly effective stray-light suppression due to the weakness of the coronal radiation. Figure 1 shows the coronal intensities, in sun disk units and as a function of heliocentric height, of the broadband visible ("white") light emission by Thomson scattering of the coronal electrons and the HI Lyman-α line-mission by resonance scattering of the coronal neutral hydrogen.

From the solar limb to heliocentric heights up to three solar radii, the intensities of the HI Lyman-α and the visible-light coronae are 10^{-6} to 10^{-8}, respectively, fainter than the sunk disk intensities in the respective wavelength bandpasses (see Refs. 6 and 7). To achieve a signal-to-noise ratio of the order of 10, the required ratio between the stray-light irradiance B_{stray} (photons $\text{cm}^{-2}\,\text{s}^{-1}$) measured on the telescope focal plane to the solar disk mean irradiance B_{Sun} for the VL channel is $\frac{B_{\text{stray}}}{B_{\text{Sun}}} < 10^{-9}$ and for the UV channel is $\frac{B_{\text{stray}}}{B_{\text{Sun}}} < 10^{-7} \cdot B_{\text{Sun}}$.

This paper describes the models used for the stray-light simulation and the obtained results using the above levels for $\frac{B_{\text{stray}}}{B_{\text{Sun}}}$ as specific requirements. The derivation of the stray-light rejection needed for the science observation goals is treated in Refs. 1 and 8.

This paper is divided in four sections. Section 2 describes the optomechanical model of the telescope including the simulated coatings. Section 3 reports the models used to simulate the scattering properties due to surface microroughness, particulate contamination (PAC), and cosmetic defects.

*Address all correspondence to: Silvano Fineschi, E-mail: fineschi@oato.inaf.it

†Current address: UNSW Canberra at the Australian Defence Force Academy, Canberra, Australia

0091-3286/2018/$25.00 © 2018 SPIE

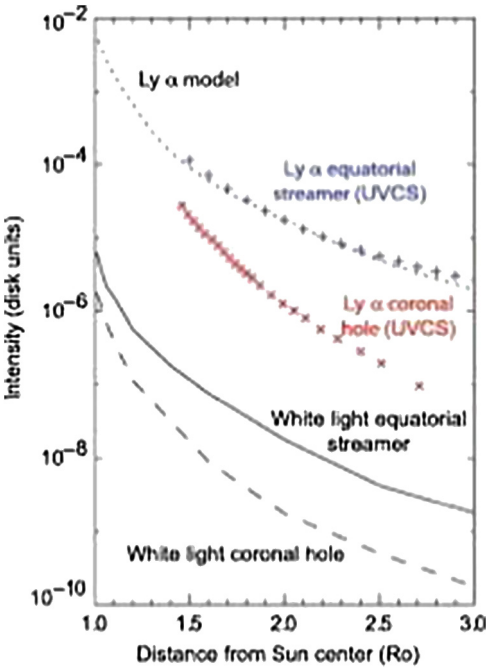

Fig. 1 Coronal intensities, in sun disk units and as a function of heliocentric height, of the broadband visible ("white") light emission by Thomson scattering of the coronal electrons and the HI Lyman-α line-mission by resonance scattering of the coronal neutral hydrogen.

Section 3 also reports a model for the simulation of diffraction. Section 4 summarizes the result of the stray-light analyses performed with Zemax OpticStudio. Section 5 compares the results obtained with two different approaches: a Monte Carlo ray trace with ASAP[5] and a semianalytical method.[6]

2 Optomechanical Model of the METIS Telescope

The results of the stray-light simulations and the compliance to the functional requirements mainly depend on how the physical properties of the objects hit by the optical rays are reproduced. Then, the maximum effort has been used in modeling all of the surfaces of the telescope to reproduce their reflecting, transmitting, absorbing, and diffusing properties.

2.1 *Geometric Model of the METIS Telescope*

Figure 2 shows the ray tracing for the UV and VL channels of METIS in the field of view (FoV) [1.5 deg, 2.9 deg]. Following the optical path, from left to right along the telescope optical axis, the solar light first encounters the IEO that defines the entrance aperture of the coronagraph. The solar

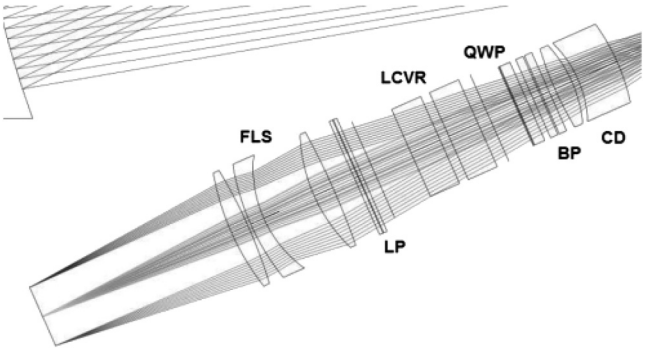

Fig. 3 Sectional view of the polarimeter lens for the VL channel with ray tracing.

light enters the boom, passing by the baffle of the shield entrance aperture (SEA), and while, the mirror M0 reflects back and dumps into space the solar disk light, the coronal light enters the telescope through the annular aperture defined by M0 and the rear of the mirror M2. The primary mirror M1 of the Gregorian telescope collects this coronal light, forming a real image of the corona along with the images of the diffracting edges of the IEO and M0. The internal occulter (IO) and the Lyot stop (LS) block these two latter images. The interference filter (IF) tilted at 12 deg with respect to the optical axis lets the UV coronal light through, onto the sensitive area of the UV detector. The UV detector has a magnesium fluoride protective window with a thickness of 4 mm. The UV channel realizes a focal length $F_{\mathrm{UV}} = 300$ mm. The IF presents a beam splitter coating identifying a second path in the telescope dedicated to the VL spectrum, presenting its optical axis tilted at 24 deg with respect to the optical axis of the UV channel.

The imaging lens of the VL channel is represented by the polarimeter lens working at finite conjugates between an intermediate focal plane of the telescope and the sensitive area of the VL detector. The VL channel realizes a focal length $F_{\mathrm{VL}} = 200$ mm.

Figure 3 shows a sectional view of the polarimeter lens with the collimating doublet (CD). The CD is an air-spaced doublet with a diameter of 27 mm, the bandpass (BP) filter made of two substrates in fused silica, the quarter wave plate (QWP), the polarimetric (PMP) group based on liquid crystal variable retarders (LCVR) cells, the linear polarizer (LP), and the focusing lens system (FLS) made of an air-spaced triplet with an outer diameter of 39 mm.

The polarizing elements (QWP, LCVR, and LP) are mounted in the Senarmont configuration[9] with the QWP presenting the fast axis at 90 deg with respect to the fast axis of

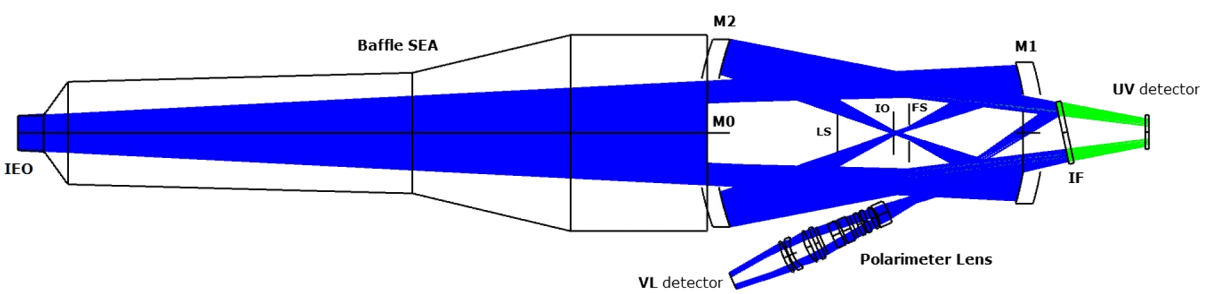

Fig. 2 Ray trace for the UV and VL channels (sectional top view).

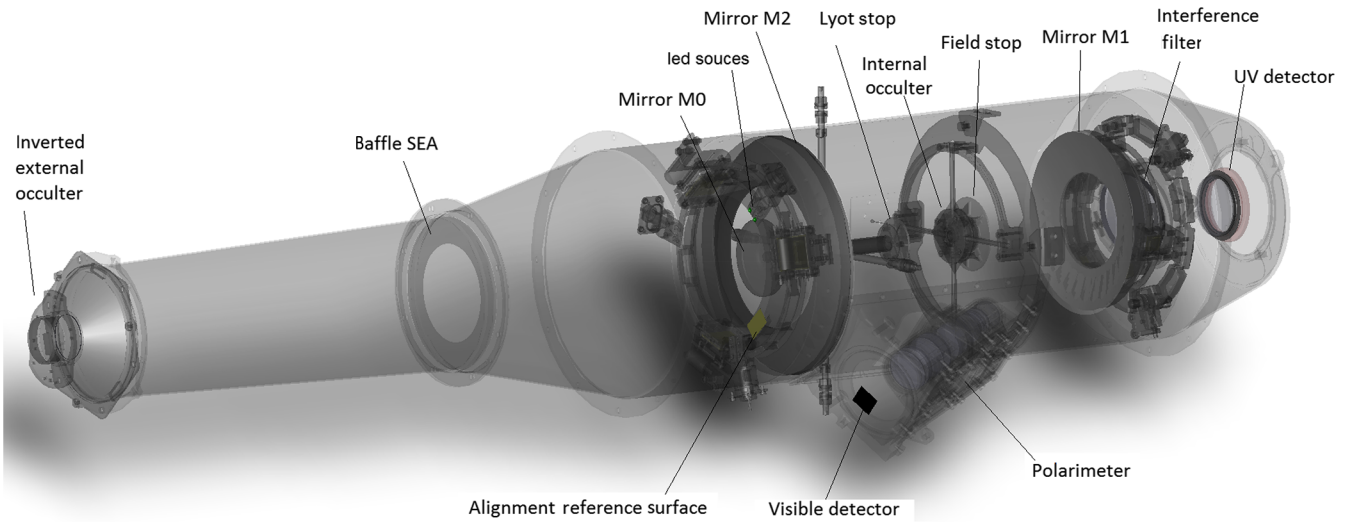

Fig. 4 Modeled telescope.

the LP and the LCVR cells having their fast axis at 45 deg with respect to the fast axis of the QWP and the LP. The nominal back focal length of the polarimeter lens is 65 mm. The QWP is made of a quartz crystalline plate (460-μm thickness) cemented onto a MgF_2 crystalline plate (370-μm thickness) cemented on a supporting lamina of fused silica with a thickness of 3.17 mm.

Using the model, Fig. 2, as a basis, a detailed optomechanical model of the telescope is simulated in the nonsequential modality of Zemax OpticStudio by importing the step files of the subassemblies and placing them at the nominal position along the optical axis (Fig. 4). Elements not necessary for the analysis as bolts and screws have not been considered.

The optomechanical model allows for a deep insight view of the instrument. Figure 5 shows the first lens of the polarimeter partially visible from the sensitive area of the UV detector (a) and the mechanical rods sustaining the IO and the mirror M0 also seen from the sensitive area of the UV detector (b).

2.2 *Model of the Coatings for the METIS Telescope*

The functional coatings deposited on the optomechanical elements of the coronagraph are simulated. Each optomechanical surface is assigned with a property of reflection, and/or transmission, and in some cases absorption as a function of the wavelength replicating the theoretical or measured coatings deposited on witness samples. The reflection and transmission of the modeled coatings are reported in Fig. 6. The theoretical curves have been provided by the suppliers of the coatings. In the first row of panels from left to right:

- the reflectivity of the metallic coating of M1 and M2 consisting of aluminium with a protective layer of magnesium fluoride working in the spectral range [120, 1000] nm;
- the antireflection coating for the lenses of the CD and FLS, for the QWP and the LP working in the spectral range [500, 700] nm;

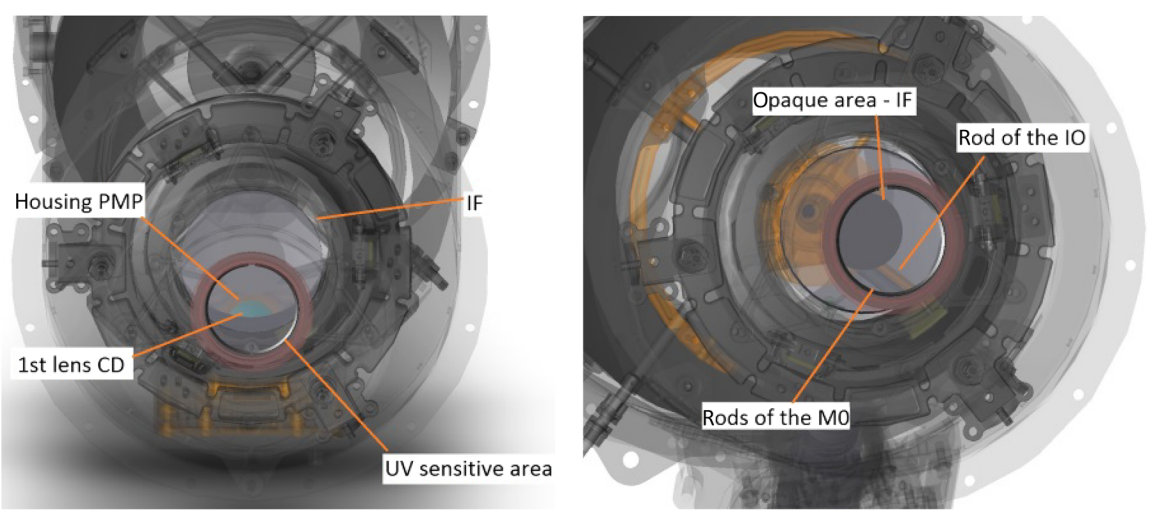

Fig. 5 (a) First lens of the polarimeter and (b) rods sustaining M0 and the IO seen from the UV detector.

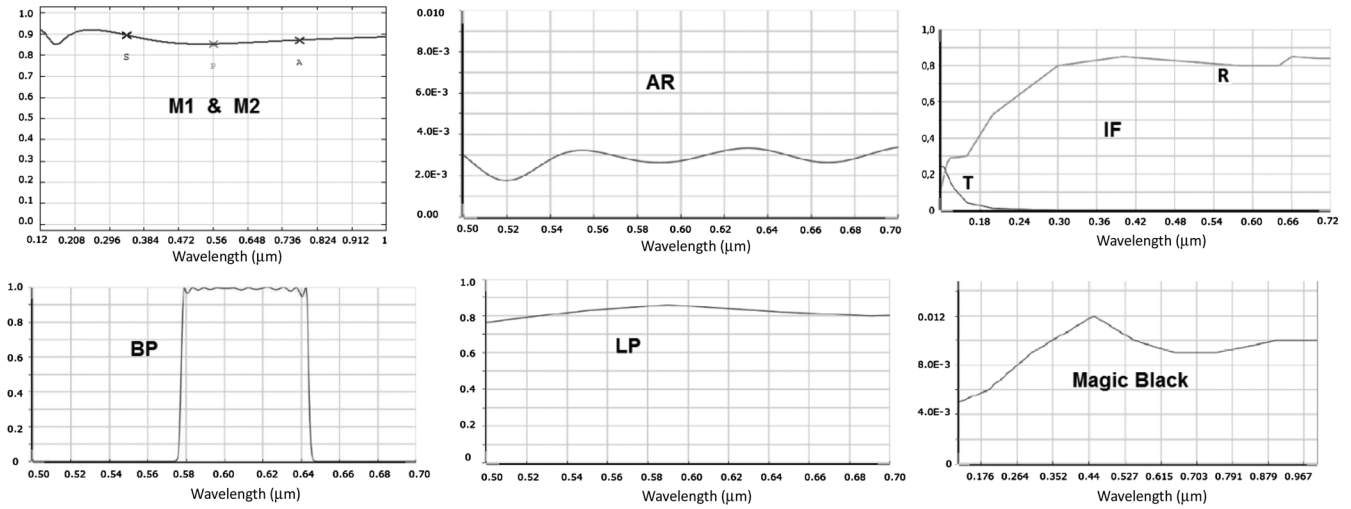

Fig. 6 Transmission and reflection curves of the modeled coatings.

- the reflection and transmission of the IF for the angle of incidence of 12 deg in the spectral range [120, 720] nm.

In the second row of Fig. 5, panels from left to right:

- the transmission of the BP filter in the spectral range [500, 700] nm;
- the transmission of the LP to polarized light parallel to the LP transmission axis in the spectral range [500, 700] nm;
- the reflectivity of the Acktar Black Magic in the spectral range [120, 700] nm.

The Acktar Black Magic coating is applied on all metallic parts and ground surfaces on the rear side of the mirrors assemblies (M0, M1, and M2).[10] The inner wall of the carbon fibre tube connecting M1 to M2 is covered with a Metal Velvet foil having similar properties to the Black Magic with reflectivity $R < 1\%$ and total integrated scattering TIS < 3%. The housing of the LCVR cells is coated with the coating Astro Black from Metal Estalki (R5%, TIS 14%). The only unblackened areas in the telescope are (i) the alignment reference surface (ARS) (with dimensions 12×20 mm^2) on the rear side of M1; (ii) the ARS (with dimensions 28×15 mm^2) on the rear side of M2 (needed for alignment purposes); (iii) the outer ground edge of the IF; and (iv) the interfaces on the protrusions machined on the rear side of the mirrors M1 and M2, dedicated to the cementing with the mechanical structural frames made of Invar.

2.3 *Model of the UV and VL Detectors*

The model of the telescope also includes the UV and VL detectors. The sensitive area of the VL detector is modeled with a reflectivity given by the complement to the quantum efficiency (QE). Figure 7 shows the measured QE of the VL detector in the spectral range [300, 800] nm with and without cover glass in the red and green curves, respectively. The upper limit fit used in the model is also shown. The UV intensifier is modeled with its uncoated MgF_2 protective window and with the mechanical parts made in white ceramic and uncoated stainless steel. The reflectivity of the white ceramic and the uncoated stainless steel parts is assumed 1% at the wavelength of 121 nm[11] with the remaining part of radiation completely absorbed. The sensitive area of the UV detector is modeled with a reflectivity of ~1% corresponding to the reflectivity of a multipore surface coated with KBr.

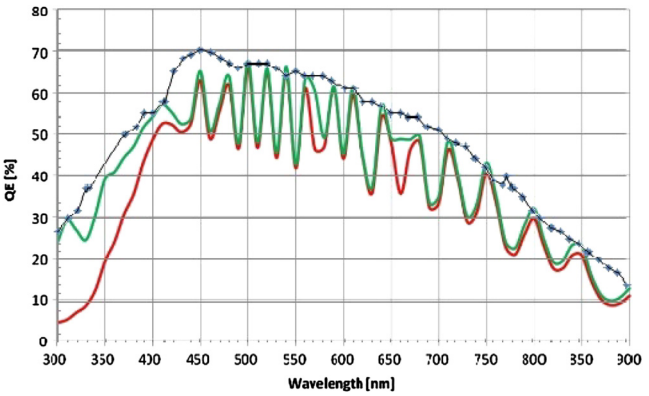

Fig. 7 QE of the VL detector. Red and green curves are measured values (by courtesy of Max Planck Institute fur Sonnensystemforschung). The continuous-dotted curve is an upper limit fit.

3 Stray-Light Analyses with Zemax Optic Studio

The sun disk light entering IEO is reflected back by M0 through IEO. The disk light diffracted by IEO or scattered by M0 enters the telescope and acts as a source of stray light. The main contributors to the stray light are represented by the surface microroughness, PAC, cosmetic defects, and diffraction due to the finite aperture of the mirror M1, the primary mirror. Using the geometric model of the telescope as a basis, four independent models are built, each one dedicated to simulate each of the four contributors.

3.1 *Stray Light Due to Surface Microroughness*

To analyze the contributor of surface microroughness, the mechanical surfaces and the optical surfaces have been provided with scattering properties. The mechanical parts of

the modeled telescope have been provided with a Lambertian scattering with a TIS equal to 0.03. This value was obtained in Ref. 12 by numerically integrating the measured bidirectional reflectance distribution function (BRDF) of the Acktar Black Magic coating of Fig. 8. These BRDF are measured at two different angles of incidence, 5 deg in (a) and 70 deg in (b), on titanium flat samples machined with a surface microroughness of 1- to 2-μm RMS and coated with different black coatings. Each plot of Fig. 8 reports the BRDF in sr^{-1} as a function of the scattering angle θ in deg. Figures 8(a) and 8(b) report the measurement for a scan along the plane of incidence on the left side and a scan perpendicular to the plane of incidence on the right side. The sample coated with Acktar Black Magic presents the lowest BRDF curve plotted in yellow color in Fig. 8

The BRDF mentioned above is a subset of the more generic bidirectional scattering distribution function (BSDF). The $\mathrm{BSDF}^{\mathrm{RMS}}(\theta)$ due to the surface microroughness of the optical surfaces of the mirrors and the lenses is simulated by means of the widely used analytical ABg model.[13,14] This scattering model is effective when scattering is mainly due to random isotropic surface roughness and the scale of the roughness is small compared with the wavelength of light being scattered, which is generally valid for polished optical surfaces.[15,16] The distribution function of a surface with a roughness RMS σ is[13,17]

$$\mathrm{BSDF}^{\mathrm{RMS}}(\theta) = \frac{\Delta n^2}{8\pi}\left[\frac{\left(\frac{2\pi}{\lambda}\right)^4 \sigma^2 L^2}{1+\left(\frac{2\pi}{\lambda} L \sin\theta\right)^2}\right] = \frac{A}{B+(\sin\theta)^g}, \tag{1}$$

with dependency of the specific parameters given by

$$A = \frac{\pi}{2}\cdot\frac{\Delta n^2 \sigma^2}{\lambda^2}, \quad B = \left(\frac{\lambda}{2\pi L}\right)^2, \quad g = 2, \tag{2}$$

where Δn is the refractive index change ($\Delta n = 2$ for mirrors) and L is the autocorrelation length. The value of the slope $g = 2$ used in our simulations is derived from Sec. 7 of Ref. 13. According to our experience, the parameters of Eq. (2) allow obtaining a reasonable prediction of the stray-light level due to surface microroughness before the manufacturing of the optical items. More accurate predictions can be obtained by fitting the measured BRDF curve, as in examples in Refs. 17–19.

The autocorrelation length is evaluated with the equation [see Eq. (2.22) of Ref. 17]

$$L = \frac{\lambda}{2\pi \sin\theta_0}, \tag{3}$$

with θ_0 being the roll-off angle. The BSDF of Eq. (1) has a high- and low-frequency asymptote in a log–log plot. The intersection of the two asymptotes allowed Wein to obtain the mentioned Eq. (2.22) in Ref. 17 for the evaluation of the autocorrelation length from the measured BSDF data.

When setting-up a model to make image quality predictions, the definition of the roll off angle plays a very crucial role depending on the optical system under consideration. Usually, the value of the autocorrelation length is taken from the literature. For example, Dittman[13] applies the value of 10 μm used by Wien,[17] which leads, through Eq. (3), to a roll-off angle θ_0 of 0.57 deg for a wavelength of 0.6328 μm. As this "standard" value of autocorrelation length can lead to BSDF plateaus that cannot be seen in actual measurements, we have adopted the approach to define the autocorrelation length such that the roll-off angle does not start within the resolution angle of the optical system under analysis. Thus for an optical system with an angular resolution θ, the roll-off angle θ_0 and subsequently the correlation length L are determined by putting $\theta = \theta_0$. By adopting this approach, the B parameter is equal for all optical items of the same channel of the METIS coronagraph. The angular resolution considered for the evaluation of L is 20 arc sec for the UV channel and 2 arc sec for the VL channel, as it results from the nominal optical design. Table 1 reports specifications for the surface microroughness σ of the optical items in their spatial frequency band limits.[14] The vendor of the optical item (Toptec) has confirmed these values by measurements with a Zygo white-light interferometer. The value of the parameters A, B, and g are calculated with Eq. (2), and the corresponding total scatter is evaluated by Zemax OpticStudio in the scattering data editor. The values for total scatter calculated by Zemax OpticStudio are in line with the values obtained through the equation $\mathrm{TIS} \approx (4\pi\sigma/\lambda)^2$ (Ref. 20), with TIS being the diffuse reflectance over the total reflectance. The calculated parameters A, B, and g are inserted in

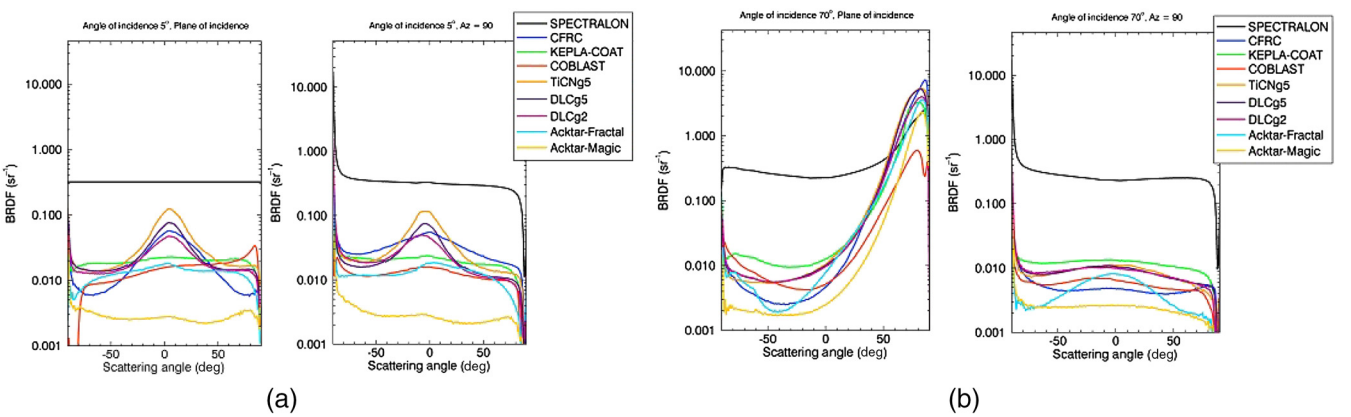

Fig. 8 Measured BRDF for AOI (a) 5 deg and (b) 70 deg for a scan along/perpendicular to the plane of incidence (left/right of each panel).

Table 1 Surface microroughness, parameters of the *ABg* model, and total scatter from Zemax OpticStudio.

Item	σ roughness	Δn	Parameters of the *ABg* model	λ (nm)	Total scatter from Zemax
Mirror M1	0.3 nm $f < 0.1$ [$1/\mu$m]	2	$A = 3.82 \times 10^{-5}$, $B = 1.04 \times 10^{-8}$, $g = 2$	121.6	0.0022059
Mirror M2	2 nm $f < 0.1$ [$1/\mu$m]	2	$A = 0.0017$, $B = 1.04 \times 10^{-8}$, $g = 2$	121.6	0.0981700
Mirror M0	0.3 nm $f > 0.1$ [$1/\mu$m]	2	$A = 3.82 \times 10^{-5}$, $B = 2.35 \times 10^{-13}$, $g = 2$	121.6	0.0033160
ARS of M1, M2	2 nm	2	$A = 0.0017$, $B = 1.04 \times 10^{-8}$, $g = 2$	121.6	0.0981700
Window of UV detector	3 nm	0.604	$A = 0.000349$, $B = 1.04 \times 10^{-8}$, $g = 2$	121.6	0.0201537
IF	1 nm	0.604	$A = 3.88 \times 10^{-5}$, $B = 1.04 \times 10^{-8}$, $g = 2$	121.6	0.0022406
Lenses in SF6G05	2 nm	0.806	$A = 1.1 \times 10^{-5}$, $B = 9.4 \times 10^{-11}$, $g = 2$	610	0.0007979
Lenses in BK7G18	2 nm	0.519	$A = 4.55 \times 10^{-6}$, $B = 9.4 \times 10^{-11}$, $g = 2$	610	0.0003300
Fused silica items	2 nm	0.458	$A = 3.54 \times 10^{-6}$, $B = 9.4 \times 10^{-11}$, $g = 2$	610	0.0002568

the scattering data editor of Zemax for the specific wavelength for which these have been calculated, allowing Zemax to automatically scale the values of A, B, and g for different wavelengths.[17]

Although mirror M1 and the IF have a different surface microroughness, respectively, 0.3 nm and 1-nm RMS, the parameter A results are approximately the same due to different values of the refractive index change Δn. Lenses in Schott BK7G18 and in SF6G05 with the same surface microroughness have different values for A due to different refractive indices.

The requirement for the surface microroughness of mirror M0 is for a spatial frequency greater than 0.1 [$1/\mu$m], so most of the reflected and scattered light due to the solar disk is rejected out of the instrument through the IEO at angles $\theta < \sin^{-1}[\lambda/(2\pi d)] \approx 0.5$ deg being λ 600 nm and $d = 1/f$. For mirrors M1 and M2, the requirement on surface microroughness is for spatial frequencies less than 0.1 [$1/\mu$m], so most of the reflected and scattered light due to the solar corona comes at angles greater than the instrumental FoV.

3.2 *Verification of the Correct Functioning of the Blocking Elements with the Sun at the Perihelion*

The first step is to compute the level of spurious light on the virtual UV and VL detectors due to the illumination coming from the solar disk when the instrument is at the minimum perihelion. This analysis has the aim to verify that all blocking elements (baffle SEA, mirror M0, LS, and IO) of the coronagraph are working properly. In this analysis, the contributor of roughness is included with all optical items modeled as reported in Table 1. The analysis is performed with the following setup:

- Sun modeled with the "source two angle" placed 1 mm out of the external edge of the IEO, with circular shape, angular extension of ± 0.954 deg (corresponding to the angular extension of the Sun at the minimum perihelion of 0.28 AU) and a normalized power equal to 1 W over the spectral range.
- Sun pointing, that is considering tilt X, $Y = 0$ (Z is the optical axis in Zemax); wavelength range $[0.12, 0.8]$ μm.
- Nominal design (nor alignment neither integration errors) of the telescope.
- Number of analysis rays $= 1 \times 10^7$.
- Minimum relative ray intensity (threshold value, $= 1 \times 10^{-15}$ W (as used by Verroi et al.[12]).

We expect that the solar disk is completely blocked by the mirror M0. In fact, the radial aperture of M0 satisfies the relation

$$R_{\mathrm{M0}} > R_{\mathrm{IEO}} + d \cdot \tan(0.954 \text{ deg}) = 33.32 \text{ mm},$$

where $R_{\mathrm{M0}} = 35.5$ mm is the radial aperture of the mirror M0, $R_{\mathrm{IEO}} = 20$ mm is the external radial aperture of the IEO, and $d = 800$ mm is the distance from the IEO to the vertex of the spherical concave mirror M0. The results of the simulation are in Fig. 9.

The results of the simulation are that no direct sun disk light reaches the virtual detectors and the intensities of the spurious rays collected on the detectors, for a source with an angular extension equal to the solar disk placed at the minimum perihelion, results of the order of magnitude of 1×10^{-13} W. Thus, the ratio stray light to sun disk light (1×10^{-13} W/1 W) is several orders of magnitude lower than the requirements. This leads to the conclusion that the blocking elements efficiently stop the sun disk. An accurate test campaign on breadboard has been carried out to evaluate the best optimization configuration for the IEO and the efficiency of the blocking element M0.[5]

The next step, described in the following sections, is to analyze the stray-light level on the coronal images.

3.3 *Stray Light Due to Surface Microroughness with the Instrumental FoV*

The instrumental stray-light level due to the surface microroughness is evaluated on the nominal design of the telescope for a sun pointing configuration. The FoV of the

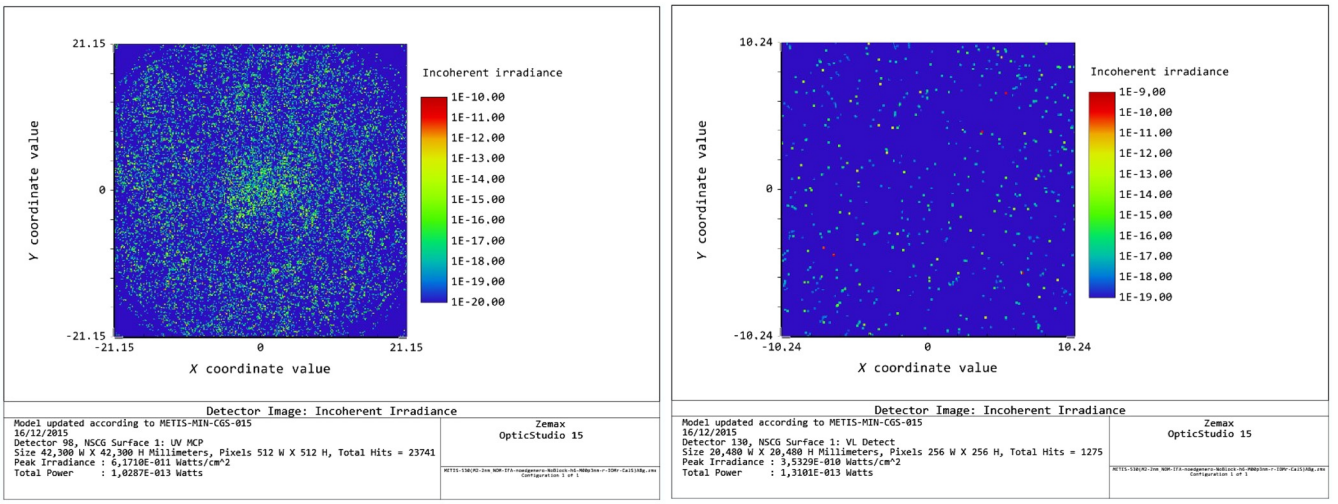

(a) (b)

Fig. 9 Stray light due to sun disk at perihelion on (a) UV and (b) VL virtual detectors in log scale for an angular extension of ± 0.954 deg and a surface roughness of mirror M0 at 0.3-nm RMS.

instrument is simulated with the "source two angle" of Zemax placed out of the entrance aperture of the telescope, with circular shape and radial aperture larger than the IEO, with angular extension equal to the FoV and with a normalized power of 1 W over a spectral range [120, 800] nm. The images on the UV and VL detectors resulting from a simulation with one million rays are reported in Figs. 10(a) and 10(b) in logarithmic scale with the corona in red and the noise in green, respectively. Letters A and B adjacent to the UV image identify a section placed at $Y = 0$ mm and at $Y = 5.5$ mm, respectively.

Figure 11 shows the simulated illumination on a plane at mirror M1 location in (a) and on plane at the IF in (b) in linear scale. Figure 11(a) shows that the illumination of mirror M1 consists of an outer ring representing the solar corona, a central ring due to the rays travelling from mirror M2 toward the IF, and a small and decentered ring representing the rays retroreflected from the IF and travelling toward the first lens of the polarimeter lens. The vignetting introduced by the four rods sustaining the mirror M0 and the IO can be seen.

Figure 12 shows the simulated irradiance profile on the UV image plane in (a) and the VL image plane in (b). For the UV channel, the black solid curve is obtained along the section AA of Fig. 10(a), and it is the result of an average of three runs of simulation. For the VL channel, the irradiance profile is along the horizontal central row of the simulated image of Fig. 10. For the UV channel, the irradiance profile is compared with the profile (dashed curve) obtained in one run of simulation with no scattering.

The simulated irradiance profile of the corona at 121.6 nm shows a higher noise in the instrumental FoV with respect to the profile in the VL. This is due to the modeled IF coating, which has a ratio of approximately 4 : 1 between the reflected and the transmitted rays ($R \approx 80\%$ in VL, $T \approx 20\%$ in UV), resulting in a lower statistics for the UV channel. A smoother intensity profile in the UV channel is obtained by combining the results of several simulations. The irradiance profiles in

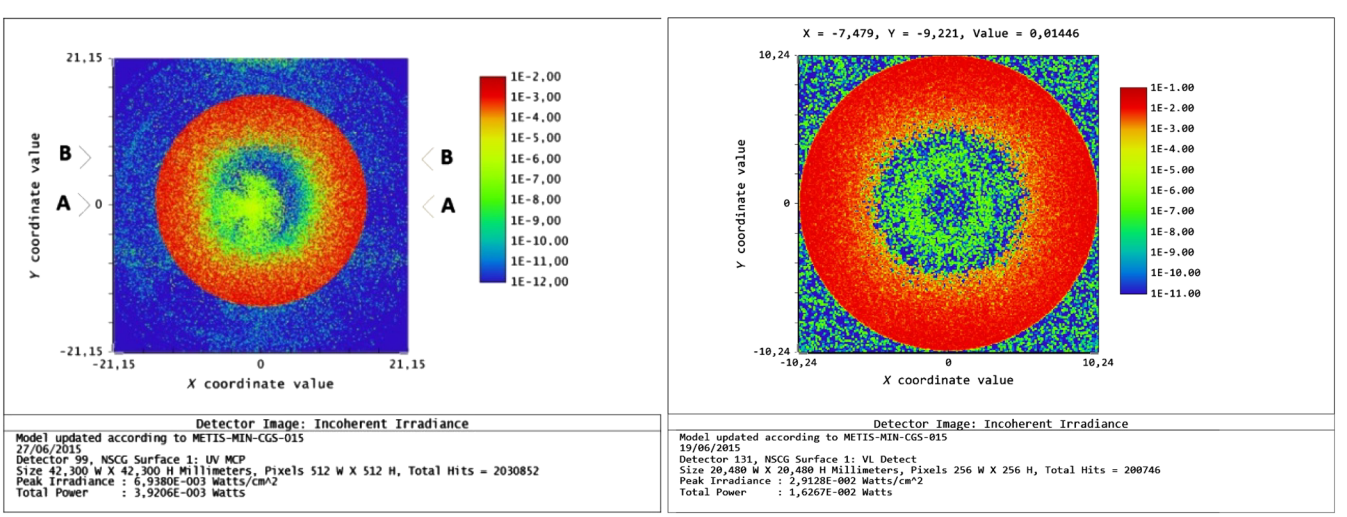

(a) (b)

Fig. 10 Simulated images on the (a) UV and (b) VL detectors in logarithmic scale.

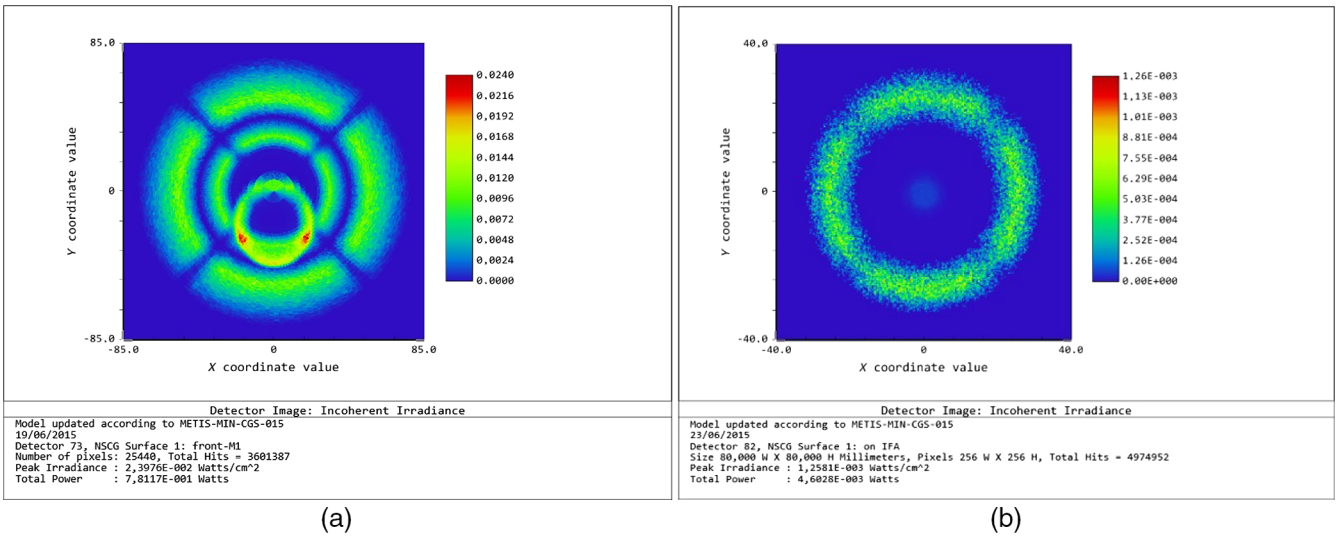

(a) (b)

Fig. 11 Simulated illumination of (a) mirror M1 and (b) IF in linear scale.

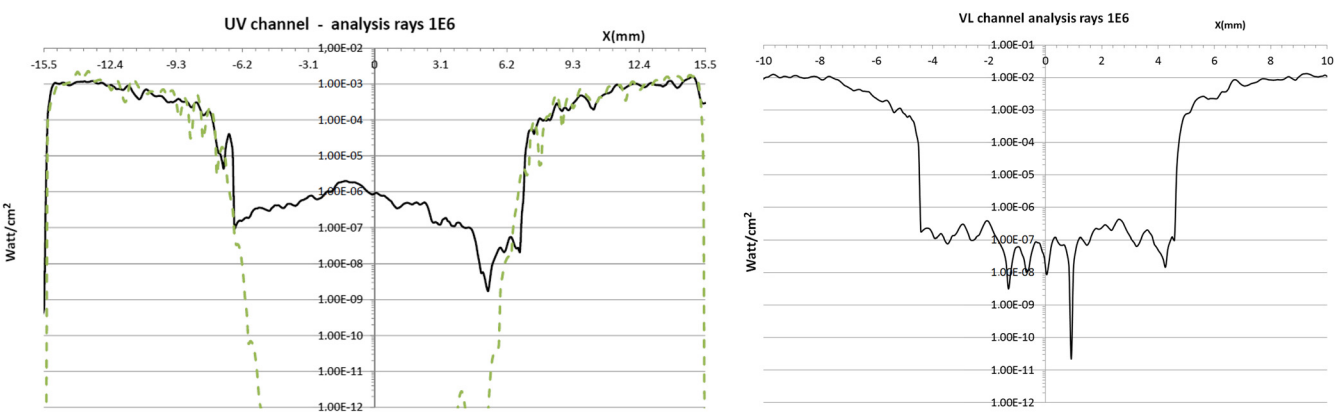

(a) (b)

Fig. 12 Simulated irradiance profile on (a) the UV detector and (b) the VL detector in logarithmic scale.

the UV and VL also show an increasing intensity as a function of the instrumental FoV reflecting the calculated vignetting function, which is maximum for high FoV. The ratio $B_{\text{stray}}/B_{\text{corona}}$ is evaluated and compared with the requirements, assuming that spurious rays are approximately uniformly distributed over the whole sensitive area of the detectors. This assumption is justified looking at the simulated irradiance on detectors of Fig. 10 where, apart from a peak placed close to the center of the UV detector, the noise is almost uniform. The average of the spurious irradiance in the UV channel is calculated along the section B–B of Fig. 10. This avoids the central peak due to rays retroreflected by the coated IF ($T \approx 20\%$, $R \approx 14\%$ at wavelength of 121.6 nm) toward the polarimeter lens, which in turn are retroreflected by the first surface of the first lens of the CD of the polarimeter.

Table 2 reports the result of the analysis on the intensity profiles of Fig. 12. The irradiance B_{stray} of the spurious rays due to surface microroughness is averaged in an interval selected in the central area of the detector limited by the inner radial aperture of the imaged corona $[F_{\text{VL}} \cdot \tan(1.5\ \text{deg}) \approx 5\ \text{mm}]$. The irradiance B_{corona} is averaged inside the imaged corona.

Considering that from Refs. 6, 21, and 22

$$(B_{\text{corona}}/B_{\text{Sun}})_{\text{UV}} \sim 5 \times 10^{-5} \quad \text{and}$$
$$(B_{\text{corona}}/B_{\text{Sun}})_{\text{VL}} \sim 1 \times 10^{-6}, \tag{4}$$

it results

Table 2 Values of the simulated irradiances and ratio $B_{\text{stray}}/B_{\text{corona}}$ due to surface microroughness.

Item	Averaged B_{stray} (W/cm^2) due to microroughness	Averaged B_{corona} (W/cm^2)	$B_{\text{stray}}/B_{\text{corona}}$
UVDA	2.29×10^{-8} in $[-4;4]$ mm along sect. B–B of Fig. 10	7.14×10^{-4}	3.20×10^{-5}
VLDA	1.32×10^{-7} in $[-4;4]$ mm	7.17×10^{-3}	1.84×10^{-5}

$$\left.\frac{B_{\text{stray}}}{B_{\text{Sun}}}\right|_{\text{UV,roughness}} \approx 1.6\times10^{-9} \quad \text{and}$$
$$\left.\frac{B_{\text{stray}}}{B_{\text{Sun}}}\right|_{\text{VL,roughness}} \approx 1.84\times10^{-11}. \tag{5}$$

The above results in Eq. (5) represent the averaged values over the whole instrumental FoV.

3.4 *Stray Light Due to Diffraction from the Finite Aperture of M1*

Fundamental to every coronagraph is the suppression of the stray light diffracted and/or scattered by the first optical element directly illuminated by the Sun.[22] In the classic Lyot coronagraph, the first optical element is the primary objective of the refractor telescope. The light diffracted by this lens is blocked by the LS. In an externally occulted reflecting coronagraph, such as the UVCS instrument[23] of the solar and heliospheric (SOHO) spacecraft[24] and METIS, the first optical element is the external occulter. The diffraction from this element is blocked by an IO. The IEO of METIS has the shape of a truncated cone (Fig. 13), where the external edge is illuminated by the sun disk and the internal edge is illuminated by diffraction and scattering.[3,5] The cone has a length of 30 mm, and the semiaperture of the cone is 1.07 deg, resulting in a larger than the angular semiextension of the sun disk at the minimum perihelion equal to 0.267 deg /0.28 AU = 0.954 deg. The diffraction of the IEO specularly reflected by mirror M1 is suppressed by the stops of the instrument, the IO, and the LS.

3.4.1 *Evaluation of the ratio $B_{\text{stray}}/B_{\text{M1}}$*

The illuminated external and internal edges of the IEO are conjugated by the mirror M1 on the plane of the IO (Fig. 14) at a radial height $Y = 2.72$ mm. The imaged edges of the IEO are then blocked by the IO having a radial aperture of 2.6 mm in the nominal design as shown in Fig. 15(a). The image is aberrated by coma and the Airy disk is a few μm as shown in Fig. 15(b).

Figure 15 shows that no geometrically traced rays can illuminate the aperture of the IO. To verify if diffractive

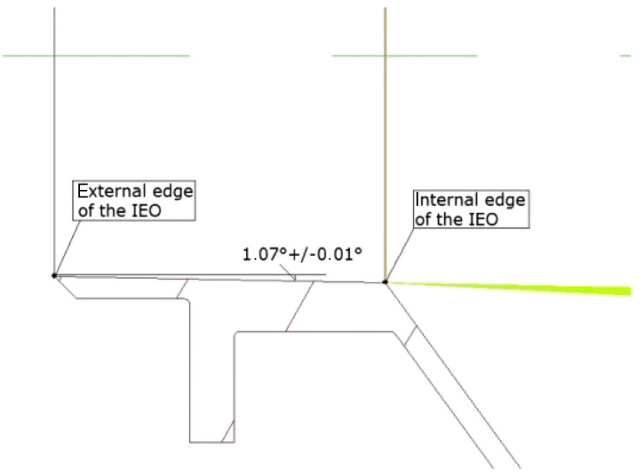

Fig. 13 Sectional view of the IEO with a label for the external and internal edges.

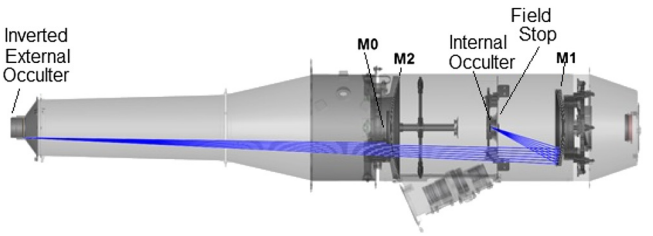

Fig. 14 Edge of the IEO conjugated by mirror M1 on the plane of the IO.

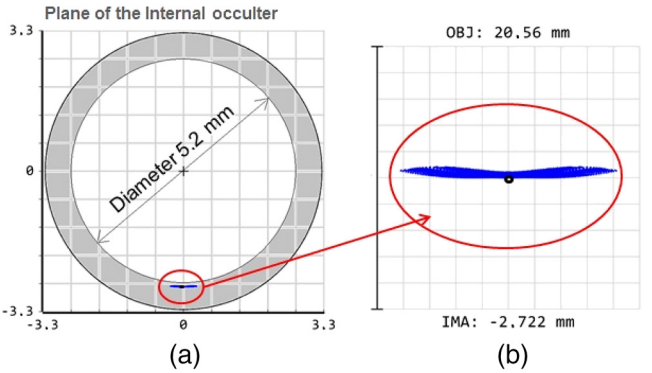

Fig. 15 Edge of the IEO conjugated by M1 on the plane of (a) the IO and (b) an enlarged view. The Airy disk represented by the black circumference is exaggerated in (b).

orders greater than one can illuminate the IO, a simplified model of the telescope is built (Fig. 16) in the nonsequential modality of Zemax. This model consists of the rear aperture of mirror M2, the mirrors M0 and M1, the FS, and the IO. In this model, all of the items are modeled as perfect surfaces having no surface microroughness and no mechanical components are considered. A point object simulated with the "source two angle" of Zemax is placed at a height of 20.56 mm corresponding to the nominal radial aperture of the internal edge of the IEO. The source is assigned with a power of 1 W and a numerical aperture (NA) in the object space equal to 0.032, large enough to illuminate mirror M1 with a margin.

A rectangular virtual detector with dimensions 5.6×5.6 mm^2 is placed on the plane of the IO. The detector is divided in 1024×1024 pixels, and the coherent data type analysis in the nonsequential modality of Zemax is switched on. To account for diffraction effects, Zemax OpticStudio computes the real and imaginary parts of the electric field using the intensity and phase of the ray referenced to the center of each pixel hit. The real and imaginary parts are then summed for many rays that strike the same pixel and the squared amplitude is summed with its phase obtaining the diffraction pattern. In our opinion, this approach allows decomposition of the diffracted radiation on the IO into a set of plane waves, thus solving the problem of Fraunhofer diffraction, in accordance with the method identified by Toraldo di Francia.[22,25] The result of a nonsequential ray tracing with one million of analysis rays is shown in Fig. 17. The orange circumference inside the blue rectangular detector of Fig. 17(a) represents the nominal aperture of the IO with a diameter of 5.2 mm. Figure 17(b) shows an enlarged view of

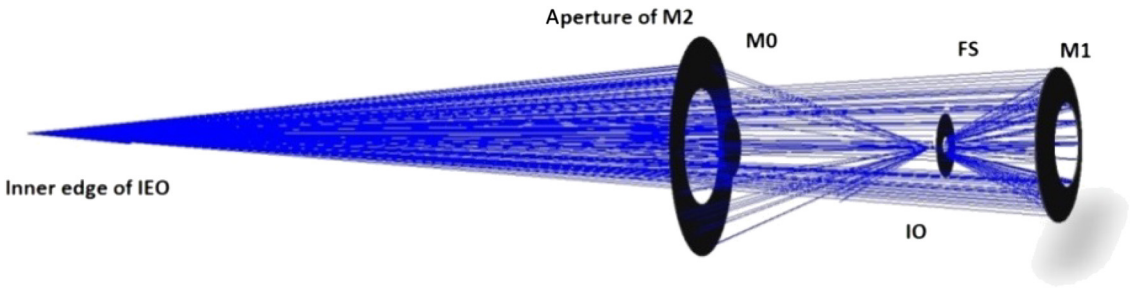

Fig. 16 Simplified model of the telescope for the analysis of diffraction.

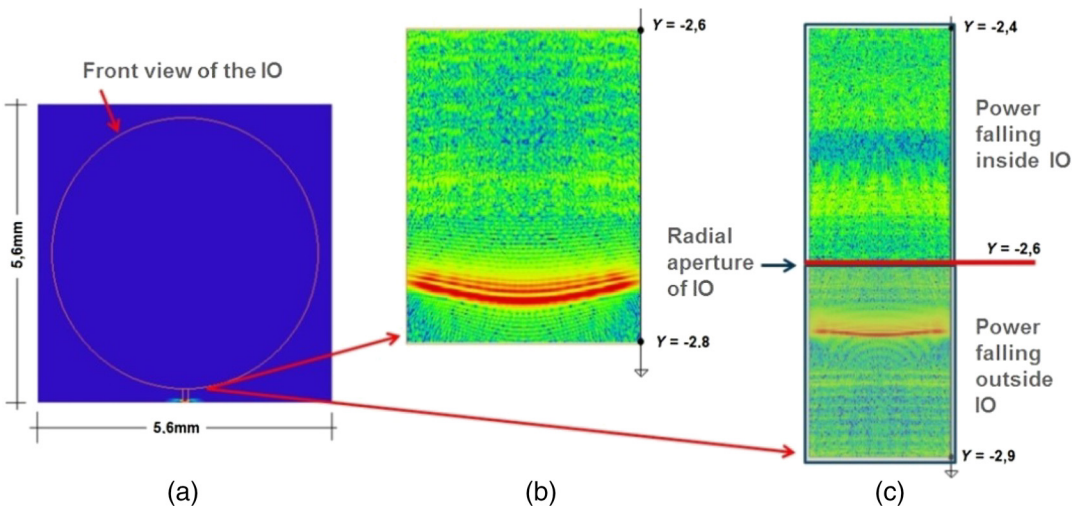

Fig. 17 (a) Image of the illuminated point object on the plane of the IO. (b) Enlarged views of a small area containing the image in log scale. (c) Power falling inside the aperture of the IO in log scale.

a small area with dimensions 0.15×0.20 mm^2 centered at $Y = -2.70$ mm. Figure 17(c) shows an enlarged view of an area with dimensions 0.20×0.50 mm^2 centered on the radial aperture of the IO at $Y = -2.60$ *mm* represented by a red horizontal line. The bottom part of the detector is in shadow as rays are blocked by the IO, whereas the upper part of the detector collects rays falling inside the aperture of the IO. The vertical Y coordinate in Figs. 17(b) and 17(c) represents the vertical distance from the optical axis of the instrument.

Figure 18 shows the calculated diffraction pattern on a detector with dimensions 0.15×0.20 mm^2 centered at $Y = -2.70$ mm for three different wavelengths: (a) 121 nm, (b) 580 nm, and (c) 632 nm. The simulated pattern changes for different wavelengths as is expected due to diffraction.

Figure 19 shows the irradiance profile in logarithmic scale on the plane of the IO as a function of the distance from the optical axis obtained with one illuminated object point placed on the internal edge of the IEO. The vertical line of Fig. 19 placed at $Y = -2.6$ mm represents the radial aperture of the IO, and the vertical line at $Y = 0$ represents the optical axis. The high intensity peak placed at $Y = -2.7$ mm is the imaged point object.

The aperture of the IO is illuminated by diffraction. The intensity is evaluated by means of two detector surfaces with circular shape, both centered on the optical axis. The first detector has a radial aperture of 2.8 mm, and the second has a coronal aperture extending from 2.6 to 2.8 mm. The two detector surfaces are placed on the plane of the IO. The difference in the intensities collected by these two detectors is the power falling inside the aperture of the IO due to diffraction for a one single illuminated object placed on the inner edge of the IEO. The problem of diffraction is solved when the diffracted light can be decomposed into a set of plane waves.[22] The nonsequential modality of Zemax, set to coherent data, evaluates the real and imaginary parts of the electric field of the ray, hitting each pixel of the virtual detector starting from the imaged point. Then, Zemax calculates the squared amplitude with its phase simulating the diffraction pattern. A single circular detector extending from 0 to 2.6 mm will not do the job as it does not contain the imaged point object.

The result is then scaled for the ratio of the solid angle identified by the NA used in the ray tracing to the solid angle 2π rad in which diffraction occurs. Then, by convolving the single-point diffraction profile (Fig. 19) by the similar adjacent profiles all along the circumference of the IEO, we obtain an estimate of the power passing beyond the IO due to diffraction for UV and VL channels

$$B_{\mathrm{IO,VL}} = B_{\mathrm{simulated,VL}} \cdot \frac{\Omega_{\mathrm{model}}}{\Omega_{\mathrm{total}}} = 4.2 \times 10^{-7}\ \mathrm{W}, \tag{6}$$

$$B_{\mathrm{IO,UV}} = B_{\mathrm{simulated,UV}} \cdot \frac{\Omega_{\mathrm{model}}}{\Omega_{\mathrm{total}}} = 4.16 \times 10^{-7}\ \mathrm{W}, \tag{7}$$

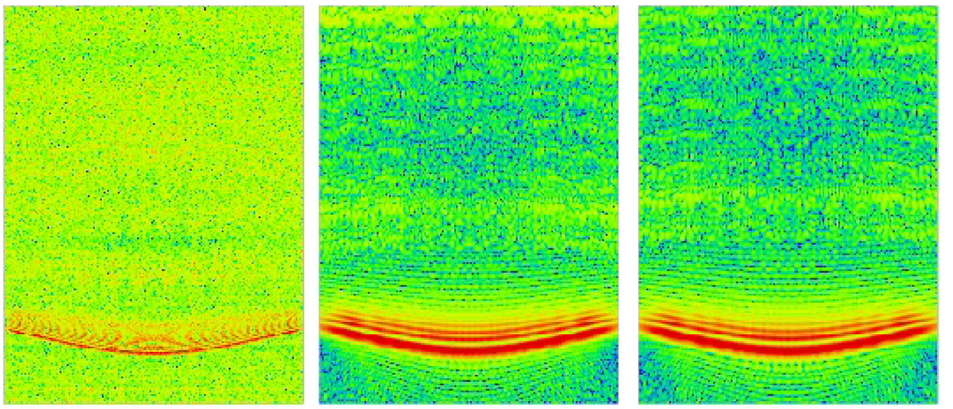

Fig. 18 Simulated diffraction pattern on a rectangular detector with dimensions 0.15×0.20 mm^2 centered at $Y = -2.7$ mm on the plane of the IO for the wavelength of (a) 121 nm, (b) 580 nm, and (c) 632 nm.

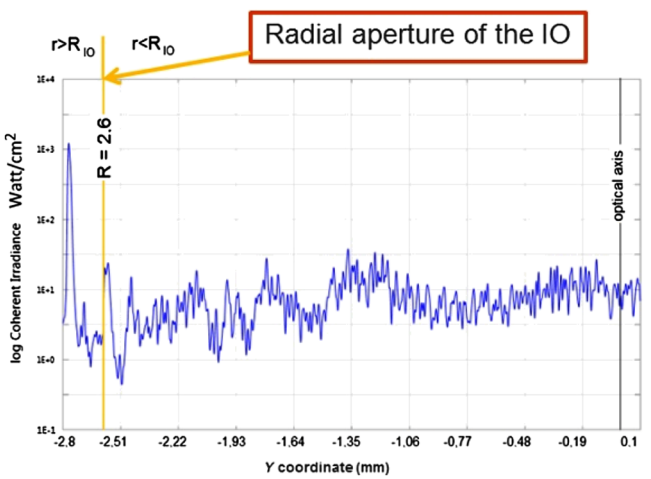

Fig. 19 Irradiance profile on the IO in log scale as a function of the distance from the optical axis.

where Ω_{model} is the solid angle identified by the object NA of the model and $\Omega_{\text{total}} = 2\pi$. The above values in Eqs. (6) and (7) represent the average of five simulations, each one performed with 1×10^6 analysis rays. The calculated radiance B_{IO} at the plane of the IO should be propagated toward the focal planes considering the throughput of the VL and UV channels. Nevertheless in the requirement $B_{\text{stray}}/B_{\text{Sun}}$, the radiance B_{sun} is intended to be measured on the focal plane and not at the entrance aperture of the telescope. Thus, B_{Sun} should also be propagated toward the detectors, and the ratio of B_{UV} and B_{VL} to B_{Sun} is equal to the ratio calculated with B_{IO}. Then, the calculated ratio of the power on the detectors to the power on mirror M1 is given by

$$\left.\frac{B_{\text{stray}}}{B_{\text{M1}}}\right|_{\text{UV,diffr.}} = \frac{4.2 \times 10^{-7}}{0.637} = 6.59 \times 10^{-7} \left.\frac{B_{\text{stray}}}{B_{\text{M1}}}\right|_{\text{VL,diffr.}} = \frac{4.16 \times 10^{-7}}{0.637} = 6.54 \times 10^{-7}, \tag{8}$$

where $B_{\text{M1}} = 6.37 \times 10^{-1}$ W derives from the simulation.

3.4.2 *Measured ratio B_{M1}/B_{Sun}*

The ratio of stray-light irradiance on mirror M1 to the sun disk irradiance has been measured with a breadboard of the occulter assembly (BOA) during an accurate test campaign dedicated to identifying the best shape for the IEO.[5] Figure 20(a) shows the design principle consisting of the IEO, the mirror M0, and a photodiode (PD). The mirror M0 and the PD are placed in the breadboard in the same position that will be occupied by mirror M0 and mirror M1 in the telescope. Figure 20(a) shows a picture of the experimental setup used in the measurement with the breadboard placed in front of a sun simulator. Figure 20(b) shows the results of the measurements reporting on the ordinate axis, the normalized intensity as a function of the PD position expressed in millimeters in a direction perpendicular to the optical axis. The maximum value of the abscissa, 80 mm, corresponds to the radial aperture of the mirror M1. The dotted curve is obtained with an IEO shaped as a simple edge; the other curves are obtained with an IEO shaped as a truncated cone with a length of 30 mm having different angles of semiaperture from 0.28 deg to 1.076 deg. The campaign allowed the selection of the semiaperture of the IEO at 1.07 deg as the most suitable for stray-light rejection in Metis.[5]

The upper limit of the measured ratio of stray-light irradiance on mirror M1 to the solar disk irradiance results $B_{\text{M1}}/B_{\text{Sun}} \approx 1 \times 10^{-4}$. By combining together the calculated $B_{\text{stray}}/B_{\text{M1}}$ with the $B_{\text{M1}}/B_{\text{Sun}}$ measured on a breadboard, we finally obtain for the ratio B_{stray} to B_{Sun}:

$$\left.\frac{B_{\text{stray}}}{B_{\text{Sun}}}\right|_{\text{UV,diffr.}} = 6.59 \times 10^{-11} \left.\frac{B_{\text{stray}}}{B_{\text{Sun}}}\right|_{\text{VL,diffr.}} = 6.54 \times 10^{-11}, \tag{9}$$

which represents the contributor to the stray light due to diffraction averaged over the whole instrumental FoV. In the above calculations, we assumed to have the same measured ratio $B_{\text{M1}}/B_{\text{Sun}}$ for the UV channel although it has been measured only for VL.

As a cross-check of our approach of simulating the stray light with Zemax OpticStudio in nonsequential modality, we use it to model the diffraction off the simple edge of

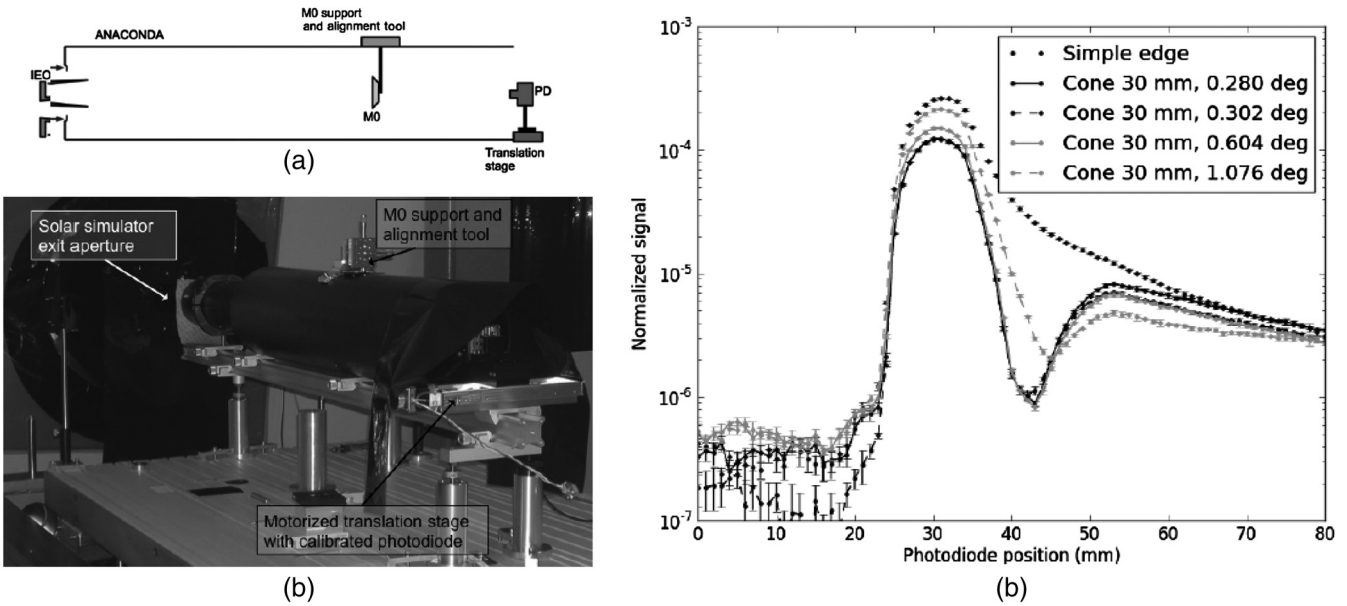

Fig. 20 (a) Design principle, (b) experimental setup, and (c) measured ratio of stray-light irradiance on M1 to sun disk irradiance.

the BOA. The simulation reported in Fig. 21 reproduces the behavior of the stray-light profile measured on the M1 plane of the BOA [cf. Fig. 20(b)].

3.5 *Stray Light Due to Particulate Contamination*

The contributor to the stray light due to PAC is analyzed with the model of Spyak and Wolfe.[13,26] The $\mathrm{BSDF}_{\mathrm{SW}}$ due to a value f of PAC as a function of the scattering angle θ is given by the equation derived from Spyak and Wolfe

$$\mathrm{BSDF}_{\mathrm{SW}}^{\mathrm{PAC}} = f \cdot \left[\frac{0.15}{0.01+\theta^{1.2}} + \frac{6\times 10^{-5}}{10^{-7}+\theta^{4}}\right]. \tag{10}$$

The magenta-dashed curve of Fig. 22 is obtained for a particle obscuration $f = 3.3$ ppm representing the requirement for METIS at the beginning of life (BOL). This curve is then fitted with the analytical ABg model with the parameters $A = 4\times 10^{-7}$, $B = 2\times 10^{-4}$, and $g = 2.2$ obtaining the blue dot-dashed curve. The fitting parameters are inserted into the scattering data editor of Zemax OpticStudio for the wavelength of 632.8 nm, which is the wavelength used by Spyak and Wolfe in their measurements.[26] The scattering from mechanical items is not considered. In the model, the mirror M0 is provided with values equal to those applied to mirrors M1 and M2, as the three mirrors share the same requirement for cleanliness levels. The simulation is performed with one million analysis rays. In Fig. 22, we also report, with the red curve, the $\mathrm{BSDF}_{\mathrm{LP}}$ of the model of Lallo and Petro[27] given by

$$\mathrm{BSDF}_{\mathrm{LP}}^{\mathrm{PAC}} = \mathrm{fit}(\theta)\frac{f}{0.00298}\left\{1+\left[\left(\frac{10.6}{\lambda}\right)^{1.8}-1\right] \cdot e^{-\left\{1.3\cdot\left[\log\left(\frac{\theta}{0.3}\right)\right]^2+3\cdot\log(\theta)+0.5\right\}}\right\}. \tag{11}$$

The function $\mathrm{fit}(\theta)$ in Eq. (10) is a fitting curve of the measurements made in Ref. 28 at the wavelength of 10.6 μm for a cleanliness level of 500

$$\log_{10}[\mathrm{fit}(\theta)] = B + a\cdot\left\{\frac{[\log_{10}(\theta)-X_1]^2}{k}\right\}^{\alpha} + b\cdot\left\{\frac{[\log_{10}(\theta)-X_2]^2}{p}\right\}^{\beta}, \tag{12}$$

where $B=-1.213$, $a=-0.891$, $X_1=0.043$, $\alpha=0.730$, $b=0.546$, $X_2=0.139$, $\beta=13.333$, $k=0.841$, and $p=3.071$.

The results of the simulation averaged on three runs for UV channel are reported in Table 3. The values at end of life (EOL) are obtained by scaling the BOL values for the ratio $f_{\mathrm{EOL}}/f_{\mathrm{BOL}} = 31$ ppm/3.3 ppm $\cong 9.4$.

Considering the ratio $B_{\mathrm{corona}}/B_{\mathrm{Sun}}$ given by Eq. (4), the results for BOL and EOL, respectively, are

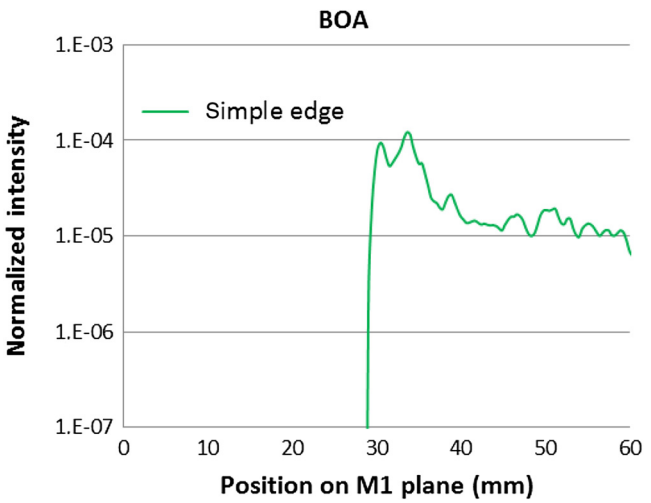

Fig. 21 Simulated level of stray light on the M1 plane ($B_{\mathrm{M1}}/B_{\mathrm{Sun}}$) due to the diffraction off the simple edge of the BOA. The simulation reproduces the behavior of the stray-light profile measured on the M1 plane of the BOA [cf. Fig. 20(c)].

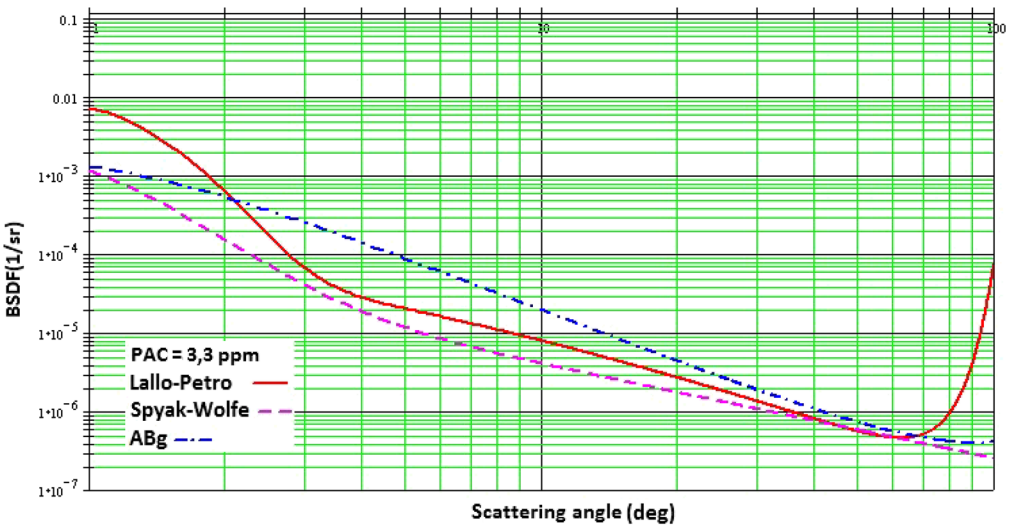

Fig. 22 BSDF due to PAC of 3.3 ppm according to model of Spyak and Wolfe (dashed magenta curve) fitted with the *ABg* model (dot-dashed blue curve) for λ 632.8 nm. BSDF according to the model of Lallo–Petro (red curve).

Table 3 Simulated irradiance and ratio B_{stray}/B_{corona} due to PAC.

Item	Averaged B_{stray} (W/cm^2) due to PAC	Averaged B_{corona} (W/cm^2)	B_{stray}/B_{corona} BOL	B_{stray}/B_{corona} EOL
UVDA	2.15×10^{-8} in $[-4;4]$ mm	7.63×10^{-4}	2.81×10^{-5}	2.64×10^{-4}
VLDA	1.81×10^{-7} in $[-4;4]$ mm	7.37×10^{-3}	2.47×10^{-5}	2.32×10^{-4}

$$\left.\frac{B_{stray}}{B_{Sun}}\right|_{UV,PAC-BOL} \approx 1.41\times10^{-9} \quad \text{and}$$
$$\left.\frac{B_{stray}}{B_{Sun}}\right|_{VL,PAC-BOL} \approx 2.47\times10^{-11}, \tag{13}$$

$$\left.\frac{B_{stray}}{B_{Sun}}\right|_{UV,PAC-EOL} \approx 1.12\times10^{-8} \quad \text{and}$$
$$\left.\frac{B_{stray}}{B_{Sun}}\right|_{VL,PAC-EOL} \approx 2.32\times10^{-10}. \tag{14}$$

The results in Eqs. (13) and (14) represent the values averaged over the whole FoV of the instrument.

3.6 *Stray Light Due to Cosmetic Defects*

The contributor to the stray light due to cosmetic defects, scratches, and digs S/D, is analyzed with the model of Peterson[29] by assuming a worst-case scenario of S/D 20/10 for the cosmetics of the mirrors. The BSDF for the digs (diameter of the dig $d = 0.1$ mm) and the scratches (width $w = 0.02$ mm) are, respectively, given by Ref. 29

$$\mathrm{BSDF}_{digs} = \frac{N_d d^2}{4}\cdot\left[1+\frac{\pi^2 d^2}{4\lambda^2}\left(1+\frac{\sin^2\theta}{l_d^2}\right)^{-3/2}\right], \tag{15}$$

Table 4 Parameters of the *ABg* model fitting the BSDF for a scratches and digs cosmetics of 20 to 10.

Item	D (mm)	Parameters of the *ABg* model	Total scatter from Zemax
Mirror M1	163	$A = 7.2\times10^{-5}$, $B = 1\times10^{-5}$, $g = 1.5$	0.0008873
Mirror M2	219	$A = 7.2\times10^{-5}$, $B = 1\times10^{-5}$, $g = 1.5$	0.0008873
Mirror M0	71	$A = 7.2\times10^{-5}$, $B = 1\times10^{-5}$, $g = 1.5$	0.0008873
Window of the UV detector	30	$A = 1.1\times10^{-4}$, $B = 1\times10^{-5}$, $g = 1.5$	0.0013463
Interferential filter	80	$A = 8.5\times10^{-5}$, $B = 1\times10^{-5}$, $g = 1.5$	0.0010403
CD, BP, QWP, and PMP	27	$A = 1.65\times10^{-4}$, $B = 1\times10^{-5}$, $g = 1.5$	0.0020194
LP, focusing lens system	39	$A = 1.1\times10^{-4}$, $B = 1\times10^{-5}$, $g = 1.5$	0.0013463

$$\mathrm{BSDF}_{scratches} = \frac{N_s w l}{\pi}\cdot\left[1+\frac{\pi w l}{\lambda^2}\left(1+\frac{\sin^2\theta}{l_s^2}\right)^{-3/2}\right], \tag{16}$$

where $N_d = \frac{1}{5\pi D}$ and $N_s = \frac{1}{\pi l D}$ are the densities of the digs and the scratches, respectively, D is the diameter of the optical item, and $l = s_{max}D$. The roll-off angles are evaluated with the equations $l_d = \left(\frac{4}{\pi^4}\right)^{1/3}\frac{\lambda}{d}$ and $l_s = \left(\frac{1}{2\pi^2}\right)^{2/3}\frac{\lambda}{(w^2 l)^{1/3}}$. The evaluated BSDF functions for the scratches and the digs are summed, and the resulting curve is fitted with an analytical *ABg* model for each optical element. Table 4 reports the optical item considered with the clear aperture, the parameters A, B, and g, and the total scatter evaluated

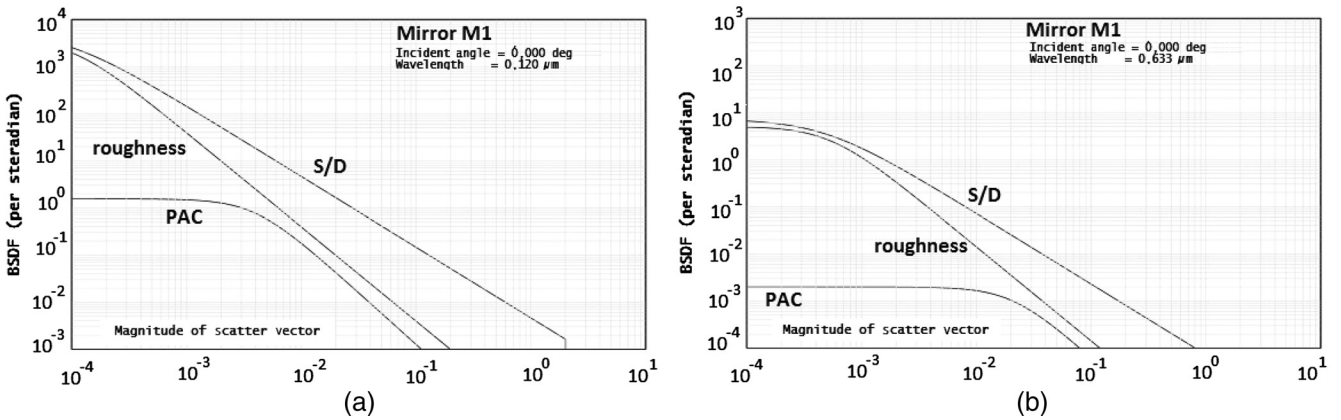

Fig. 23 Modeled BSDF curves as a function of the scattering angle for M1 at wavelength of (a) 121 nm and (b) 633 nm.

by Zemax OpticStudio. The wavelength used in the calculation is 632.8 nm.

Figure 23 shows the modeled BSDF (sr^{-1}) of the mirror M1 as a function of the magnitude of the scatter vector. This is the difference between the specularly reflected ray and the scattered ray projected in the plane of incidence for the three contributors of surface microroughness, cosmetic defects (S/D), and PAC at BOL. The curves of Fig. 23(a) are for the wavelength of 121 nm, and the curves of Fig. 23(b) are for the wavelength of 633 nm. The values of the parameters A, B, and g of Table 4 inserted in the scattering data editor of Zemax for the specific wavelength of 632.8 nm are automatically scaled by Zemax OpticStudio for different wavelengths.

The parameters A, B, and g of Table 4 are applied to the optical surfaces of the modeled telescope and a simulation is run with 2×10^5 analysis rays. No contributor from mechanical surfaces is considered. The results of the simulation averaged on three runs for the UV channel are summarized in Table 5.

Considering the ratio $B_{\text{corona}}/B_{\text{Sun}}$ given by Eq. (4), we obtain

$$\left.\frac{B_{\text{stray}}}{B_{\text{Sun}}}\right|_{\text{UV,S-D}} \approx 1.58 \times 10^{-9} \quad \text{and}$$
$$\left.\frac{B_{\text{stray}}}{B_{\text{Sun}}}\right|_{\text{VL,S-D}} \approx 2.12 \times 10^{-11}. \tag{17}$$

The result in Eq. (17) represents the value averaged over the whole FoV of the instrument.

Table 5 Simulated irradiance and ratio $B_{\text{stray}}/B_{\text{corona}}$ due to cosmetic defects.

Item	Averaged B_{stray} (W/cm^2) due to cosmetics	Averaged B_{corona} (W/cm^2)	$B_{\text{stray}}/B_{\text{corona}}$
UVDA	2.31×10^{-8} in $[-4;4]$ mm	7.32×10^{-4}	3.15×10^{-5}
VLDA	1.64×10^{-7} in $[-4;4]$ mm	7.69×10^{-3}	2.12×10^{-5}

4 Results for the Stray Light

The curves $B_{\text{stray}}/B_{\text{Sun}}$ derived from the simulated irradiance profiles are reported in Fig. 24 as a function of the instrumental FoV for (a) the UV and (b) VL focal planes at the distance

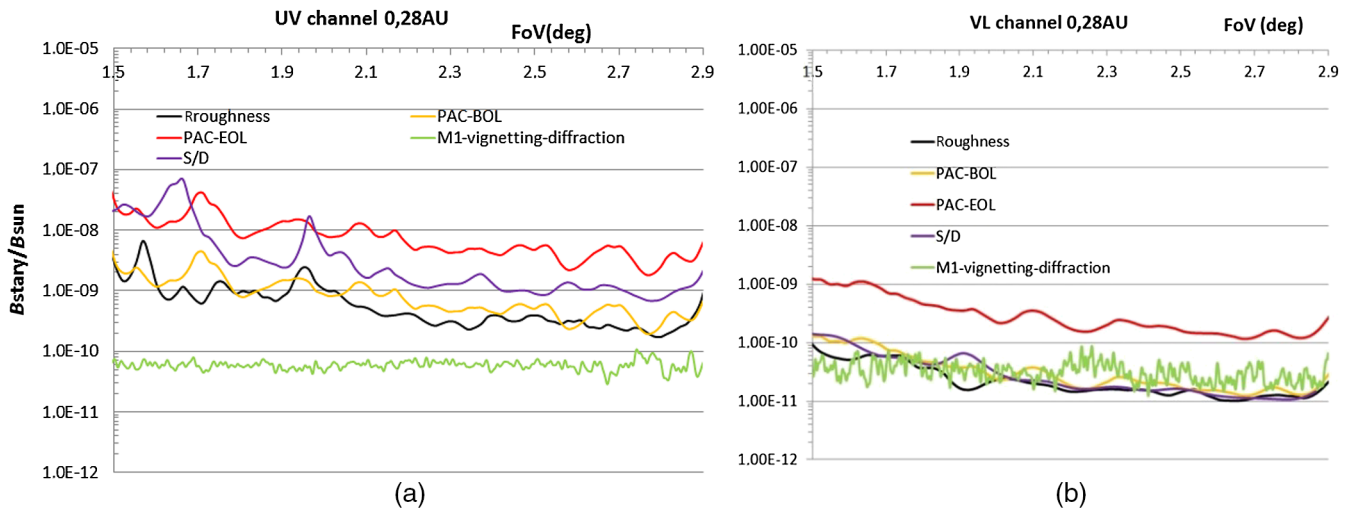

Fig. 24 Contributors to stray-light level on the (a) UV and (b) VL focal planes.

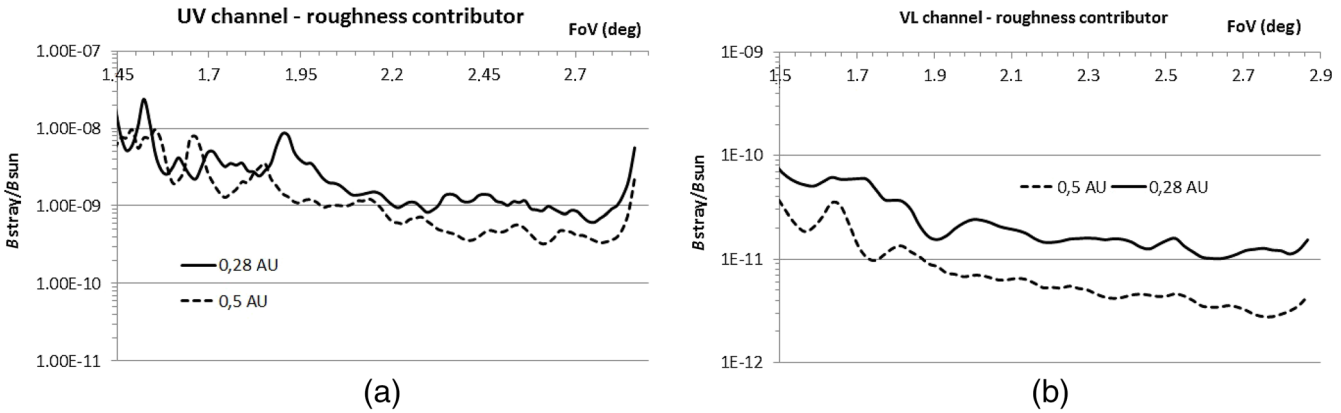

Fig. 25 Contributor of surface microroughness on the (a) UV and (b) VL focal planes at 0.28 AU (solid curve) and at 0.5 AU (dashed curve).

of minimum perihelion (0.28 AU). The light green curve represents the diffraction, the black curve the surface microroughness, the yellow and red curves the PAC BOL and EOL, respectively, and the violet curve the cosmetic defects. The calculated $B_{\text{stray}}/B_{\text{Sun}}$ due to surface microroughness for two different distances from the Sun, 0.28 and 0.5 AU, is reported in Fig. 25. The higher level of noise in the UV channel with respect to the VL channel is due to the lower statistics generated by the beam splitter coating of the IF.

The ratio $B_{\text{stray}}/B_{\text{Sun}}$ results $<10^{-7}$ for the UV channel and $<10^{-9}$ for the VL channel, thus being compliant to the requirements of stray light.

The stray-light level due to sun disk illumination at minimum perihelion has also been evaluated with the mirror M0 presenting a relaxed surface microroughness of 2-nm RMS instead of 0.3-nm RMS in the frequency band limit $f > 0.1$ $[1/\mu\text{m}]$. The result is shown in Fig. 26.

Table 6 reports the results for the sun disk stray light at minimum perihelion obtained with two values of surface

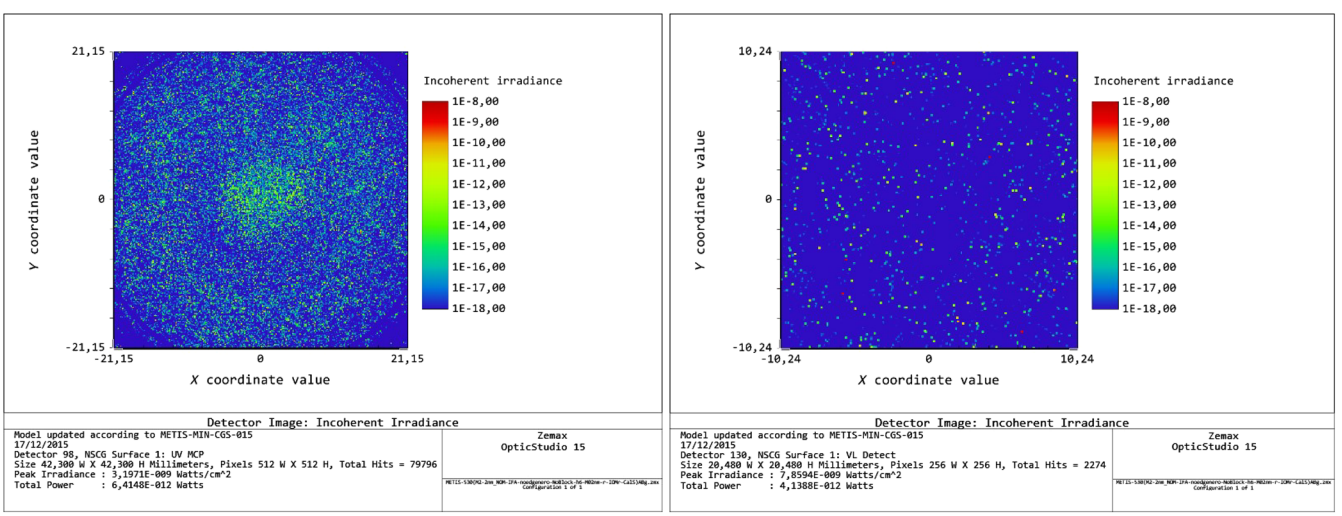

Fig. 26 Stray light due to sun disk at perihelion on (a) UV and (b) VL virtual detectors in log scale for an angular extension of ± 0.954 deg and a surface roughness of mirror M0 at 2-nm RMS.

Table 6 Stray light due to sun disk illumination for two different values of surface microroughness of M0.

Analysis rays 1×10^7—angular extension of the source $= \pm 0.954$ deg—input power 1 W

Roughness of mirror M0 (nm RMS)	UV image plane		VL image plane	
	No. of collected rays	Collected power (W)	No. of collected rays	Collected power (W)
2	79,796	6.4148×10^{-12}	2274	4.1388×10^{-12}
0.3	23,741	1.0287×10^{-13}	1275	1.3101×10^{-13}

microroughness of mirror M0 in simulations performed with 10 millions of analysis rays. This table reports the number of collected rays and the value of power at the UV and VL image planes of the instrument. The mirror M0 faces at 800 mm the IEO, with a diameter of 40 mm (see Fig. 2). Thus, M0 views IEO under an angle of 2.9 deg [$=\tan^{-1}(40/800)$]. On the other hand, the M0 measured roughness is 0.3 nm at spatial frequencies $f > 0.1$ [$1/\mu$m]; thus, most of the scatter occurs within an angle of ~0.5 deg [$=\sin^{-1}[(\lambda/2\pi d)]$ with $\lambda = 0.6$ μm and $d = 1/f = 1/[0.1\ \mu\text{m}^{-1})]$. Therefore, the greatest part of the light scattered by the mirror M0 is rejected out of the instrument through the IEO.

With this geometry, only the rays scattered in the distribution tails of the BRDF eventually reach the detectors, while the bulk of the rays, within the BRDF "roll-off angle" (θ_0), are rejected outside the IEO and, thus, never reach the detectors. The number of rays within the BRDF "roll-off angle" depends on the surface roughness. This gives reason for the dependence on the roughness of the number of collected rays and collected power in Table 6. Indeed, these rays do not include the rays "rejected" through IEO, and, therefore, their number does not follow the law $1/\lambda^2$ that would be followed by the total number of scattered rays.

5 Conclusions for the Stray-Light Analysis

5.1 *Summary of the Stray-Light Analysis and Comparison with Monte Carlo Analysis*

The predicted levels of stray light derived from curves of Fig. 24 for the FoV of 2.2 deg are summarized in Table 7 at BOL and in Table 8 at EOL.

The results of Tables 7 and 8 obtained with Zemax OpticStudio are consistent with those obtained with two different approaches: the Monte Carlo ray trace with ASAP[12] and a semianalytical model[6] as summarized in Table 9.

Table 7 Summary of predicted BOL stray-light level obtained with Zemax OpticStudio.

	UV channel		VL channel	
BOL values minimum perihelion FoV 2.2 deg	Value	Requirement	Value	Requirement
Surface microroughness	1×10^{-9}	$<10^{-7}$	5×10^{-11}	$<10^{-9}$
Diffraction due to finite aperture of M1	9×10^{-11}		9×10^{-11}	
PAC (BOL)	1×10^{-9}		5×10^{-11}	
Cosmetic defects	1×10^{-9}		5×10^{-11}	
Total (linear sum)	$\sim3\times10^{-9}$	$<10^{-7}$	$\sim1.3\times10^{-10}$	$<10^{-9}$

Table 8 Summary of predicted EOL stray-light level obtained with Zemax OpticStudio.

	UV channel		VL channel	
EOL values minimum perihelion FoV 2.2 deg	Value	Requirement	Value	Requirement
Surface microroughness	1×10^{-9}	$<10^{-7}$	5×10^{-11}	$<10^{-9}$
Diffraction due to finite aperture of M1	9×10^{-11}		9×10^{-11}	
PAC (EOL)	1×10^{-8}		5×10^{-10}	
Cosmetic defects	1×10^{-9}		5×10^{-11}	
Total (linear sum)	$\sim1.2\times10^{-8}$	$<10^{-7}$	$\sim5.1\times10^{-10}$	$<10^{-9}$

Table 9 Summary of predicted stray-light level obtained with ASAP and with a semianalytical model.

	B_{stray}/B_{Sun} (FoV = 2 deg at 0.28 AU)				
	EOL particle contamination		No particle contamination		
Contributors and type of analysis	UV channel	VL channel	UV channel	VL channel	Reference
Microroughness with ASAP	Not available	Not available	1×10^{-9}	3×10^{-11}	12
Microroughness and contamination EOL with semianalytical model	2×10^{-9}	3×10^{-10}	Not available	Not available	5

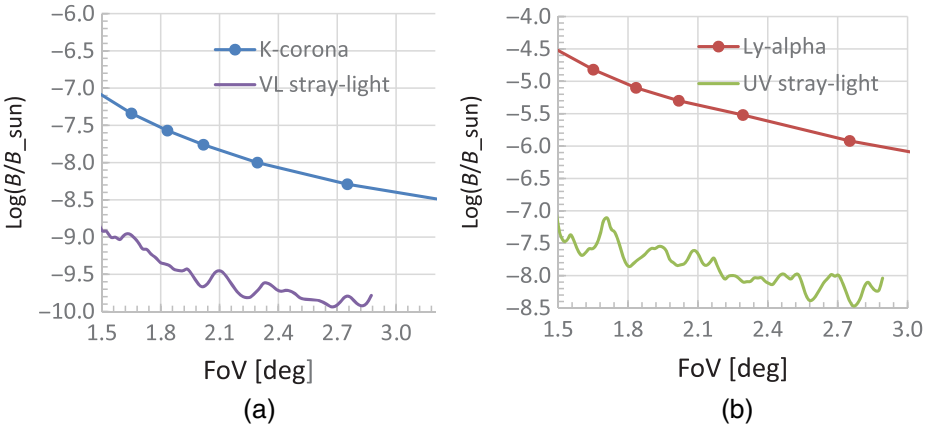

Fig. 27 (a) Brightness of the K-corona, in solar disk units across the FoV and VL stray-light level as derived by this analysis (PAC EOL, cf. Table 8). (b) Same for HI Lyman-α corona.

Taking into account that the three approaches were developed independently, the results are in considerable agreement and show compliance with the requirement of stray-light level for both the UV and VL channels.

5.2 *Coronal Signal Versus Stray Light*

The comparison of the coronal signal with the expected stray-light level gives the signal-to-noise ratio across the Metis FOV. Figure 27 shows the coronal brightness of the K-corona (a) and the HI Lyman-α (b), in solar disk units across the FoV compared with the VL and UV stray-light levels as derived by this analysis (PAC EOL, cf. Table 8).

The stray-light analysis of METIS presented here shows that the coronagraph design fulfills the requirements based on the coronal VL and UV brightness variation over the instrument FOV.

Acknowledgments

This work was funded by the ASI by industrial contract #2013-057-I.0 and by scientific contract #I/013/12/0.

References

1. S. Fineschi et al., "METIS: a novel coronagraph design for the Solar Orbiter mission," *Proc. SPIE* **8443**, 84433H (2012).
2. S. Fineschi et al., "Stray-light analyses of the METIS coronagraph on Solar Orbiter," *Proc. SPIE* **9604**, 96040K (2015).
3. S. Fineschi, "Novel optical designs for space coronagraphs: inverted occulters and Lyot-stops," in *International Conference on Space Optics*, Rhodes Island, Greece (2010), http://www.congrexprojects.com/custom/icso/Presentations%20Done/Session%205b/01_Fineschi.pdf
4. F. Landini et al., "Optimization of the occulter for the Solar Orbiter/METIS coronagraph," *Proc. SPIE* **8442**, 844227 (2012).
5. F. Landini et al., "Improved stray light suppression performance for the Solar Orbiter/METIS inverted external occulter," *Proc. SPIE* **8862**, 886204 (2013).
6. S. Fineschi et al., "Stray light analysis of a reflecting UV coronagraph/polarimeter with multilayer optics," *Proc. SPIE* **2010**, 78–92 (1994)
7. https://ase.tufts.edu/cosmos/print_images.asp?id=28
8. M. Romoli et al., "METIS: the visible and UV coronagraph for Solar Orbiter," in *Int. Conf. on Space Optics* (2014).
9. S. Fineschi et al., "KPol: liquid crystal polarimeter for K-corona observations from the SCORE coronagraph," *Proc. SPIE* **5901**, 59011I (2005).
10. F. Landini et al., "Coating and surface finishing definition for the Solar Orbiter/Metis inverted external occulter," *Proc. SPIE* **9151**, 91515H (2014).
11. F. Wooten, *Optical Properties of Solids*, Academic Press, New York (1972).
12. E. Verroi et al., "METIS-ESA Solar Orbiter mission internal stray-light analysis," in *Int. Conf. on Space Optics* (2014).
13. M. G. Dittman, "Contamination scatter functions for stray-light analysis," *Proc. SPIE* **4774**, 99 (2002).
14. J. E. Harvey et al., "Total integrated scatter from surfaces with arbitrary roughness, correlation width and incident angles," *Opt. Eng.* **51**(1), 013402 (2012).
15. J. Irizar and B. Harnich, "BRDF prediction using surface micro-roughness measurements," in *Proc. Int. Conf. on Space Optical Systems and Applications (ICSOS)* (2012).
16. J. C. Stover, *Optical Scattering: Measurement and Analysis*, 2nd ed., SPIE Optical Engineering Press, Bellingham (1995).
17. S. J. Wein, "Small-angle scatter measurement," PhD Thesis, University of Arizona, Tuscon (1989), http://arizona.openrepository.com/arizona/bitstream/10150/184794/6/azu_td_9000785_sip1_w.pdf.
18. T. T. Shara et al., "Performance of ion-figured silicon carbide SUMER telescope mirror in the vacuum ultraviolet," *Appl. Opt.* **35**(10), 1742–1750 (1996).
19. E. L. Church et al., "The prediction of BRDFs from surface profile measurements," *Proc. SPIE* **1165**, 136–150 (1989).
20. *OpticStudio User Manual*, p. 1395 (2015).
21. S. Fineschi et al., "Stray light analysis of a reflecting UV coronagraph/polarimeter with multilayer optics," *Proc. SPIE* **2010**, 78–92 (1994).
22. M. Romoli et al., "Stray-light suppression in a reflecting white-light Coronograph," *Appl. Opt.* **32**, 3559–3569 (1993).
23. J. L. Kohl et al., "The ultraviolet coronagraph spectrometer for the solar and heliospheric observatory," *Sol. Phys.* **162**, 313–356 (1995).
24. V. Domingo et al., "The SOHO mission: an overview," *Sol. Phys.* **162**, 1–37 (1995).
25. G. T. Di Francia, *La diffrazione della Luce*, Edizioni Scientifiche Einaudi, Torino, Italy, p. 97 (1958).
26. P. R. Spyak and W. L. Wolfe, "Scatter from particulate contaminated Mirrors," *Opt. Eng.* **31**(8), 1746–1784 (1992).
27. M. Lallo, "NGST Straylight," Space Telescope Science Institute, http://www.stsci.edu/hst/training/events/InfraredInstrumentation/sept99tips.fm.pdf (1999).
28. J. Y. Plesseria et al., "Guidelines for contamination control of space optical systems," CSL Technical Report UG.CSL.CLE.00001 (2001).
29. G. L. Peterson, "A BRDF model for scratches and digs, in reflection; scattering and diffraction from surfaces III," *Proc. SPIE* **8495**, 84950G (2012).

Paolo Sandri received his MS degree in physics from the University of Pisa in 1996 and his degree of the Specialization School in Optics from the University of Florence in 2001. He is an optical engineer in OHB company. His interest is in optical design and analyses (tolerancing, stray-light) and optical metrology. He has designed many instruments for industrial, medical, military, and space applications.

Silvano Fineschi is a director of the Istituto Nazionale di Astrofisica-Astrophysical Observatory Torino (Italy) with more than 25 years of experience in space-based coronagraphs. He has been involved in several solar space missions of NASA and ESA. He is the project scientist for the METIS coronagraph on the ESA Solar Orbiter and the PI of the sounding-rocket coronagraphic experiment for the NASA suborbital mission HERSHEL. He is the lead Co-I for the Italian contribution to the formation-flying coronagraph on the ESA PROBA-3.

Marco Romoli received his PhD in astronomy in 1991 with a dissertation on the UV Coronagraph Spectrometer (UVCS) for the SOHO

mission. He works mainly in the field of space instrumentation for the observation of the sun and the solar corona in the visible and UV wavebands, participating to present and future space and suborbital solar missions: SOHO, HERSCHEL, PROBA3, Solar Orbiter. He is a PI of the imaging coronagraph Metis of the Solar Orbiter payload.

Federico Landini received his PhD in astronomy in 2006 with a dissertation on the stray-light analysis for the HERSCHEL/SCORE coronagraph (successfully launched in 2009). He has been working on occulter optimization for many space-borne externally occulted coronagraphs. He designed laboratory setups for UV optical tests under vacuum, particularly aimed at UV polarimetry. Currently, he is working on instrument design for the study of the solar corona and on solar data analysis.

Giampiero Naletto is an associate professor in experimental physics at the University of Padova. He has concentrated his research activities on the realization of innovative optical instrumentation, mainly for space and ground astronomical applications. He has contributed to the development and realization of several instruments for both NASA and ESA missions, as UVCS on SOHO, FUSE, the OSIRIS imaging system on Rosetta. He is a coauthor of more than 300 publications on *International Journals and Conference Proceedings*.